Original citation:
Wu, Zhongze, Zhu, Z. Q. and Zhan, Hanlin. (2017) Comparative analysis of partitioned stator flux reversal PM machine and magnetically geared machine operating in Stator-PM and Rotor-PM modes. IEEE Transactions on Energy Conversion.

Permanent WRAP URL:
http://wrap.warwick.ac.uk/88897

A note on versions:
The version presented here may differ from the published version or, version of record, if you wish to cite this item you are advised to consult the publisher's version. Please see the 'permanent WRAP URL' above for details on accessing the published version and note that access may require a subscription.

For more information, please contact the WRAP Team at: wrap@warwick.ac.uk

warwick.ac.uk/lib-publications

Comparative Analysis of Partitioned Stator Flux Reversal PM Machine and Magnetically Geared Machine Operating in Stator-PM and Rotor-PM Modes

Zhongze Wu, Z. Q. Zhu, *Fellow*, *IEEE*, and Hanlin Zhan

Abstract– **In this paper, the partitioned stator flux reversal permanent magnet (PM) (PS-FRPM) machine and the conventional magnetically geared (MG) machine operating in both stator-PM (SPM) and rotor-PM (RPM) modes are comparatively analyzed in terms of electromagnetic performance to provide design guides for a MG machine regarding: (a) a SPM or RPM type machine and (b) a higher or lower gear ratio machine. It is found that a SPM type machine is recommended, since both PS-FRPM and MG machines operating in SPM modes have a higher phase back-EMF and hence torque than their RPM counterparts, respectively, as a result of a similar phase flux-linkage but a higher electric frequency since the iron piece number is larger than the PM pole-pair number. Moreover, a smaller gear ratio machine is preferred from the perspective of a higher power factor and hence a lower inverter power rating, as the conventional MG machines with higher gear ratios suffer from larger flux-leakage, higher synchronous reactance and hence lower power factors, as well as higher iron losses, than the PS-FRPM machines. However, higher gear ratio machines feature lower cogging torques and torque ripples due to the smaller difference between the PM pole-pair number and iron piece number. Both prototypes of PS-FRPM machine operating in SPM mode and MG machine operating in RPM mode are built and tested to verify the FE predicted results.**

Index Terms— **Flux modulated machine, flux reversal, magnetically geared (MG) machine, partitioned stator, permanent magnet (PM), power factor, rotor-permanent magnet, stator-permanent magnet.**

I. INTRODUCTION

PERMANENT MAGNET (PM) machines have been used for many applications from automotive to domestic, due to the high torque density and efficiency [1]-[5]. According to the PM locations, PM machines can be classified into two types [3], *i.e.* the rotor-PM machines having rotating PMs [4]-[7], and the stator-PM machines in which PMs are static in the stator.

For the rotor-PM machines with distributed windings having less spatial armature reaction magnetomotive force (MMF) harmonics [4], the average electromagnetic torque is generated by the fundamental air-gap field. Although the spatial armature reaction MMF harmonics caused by the modulation of stator slots in the conventional rotor-PM machines having concentrated windings can produce ~5% of the electromagnetic torque [8], the accompanying parasitic effects such as rotor losses, noise, vibration, unbalanced

magnetic pull, *etc.* are severer [9]. However, the torque component can be effectively enlarged when the modulation of stator slots is enhanced in the rotor-PM machine, which can be classified as a vernier machine [10]-[13]. As revealed in [10] and [11], the operation principle of a vernier machine is similar to a magnetic gear [14]-[17] and a magnetically geared (MG) machine [18]-[29]. The modulation of stator slots to the open-circuit PM and armature reaction fields makes them synchronous to each other, generating average electromagnetic torque.

Magnetic gear is a torque transmit device, which consists of two PM bodies and iron pieces modulating the PM MMFs [14]. Torque can be transmitted between every two parts of them, with various gear ratios being obtained [15]. However, in a magnetic gear, the torque transmission between high- and low-speed gears is conducted electromagnetically, whilst this is completed by directly contacting in a mechanical gear. Compared with a mechanical gear, gear lubrication can be exempted in a magnetic gear, and hence noise, vibration and reliability can be improved [14]. Due to the merits of magnetic gear and the electromagnetically torque transmitting, MG machines which integrate electrical machines and magnetic gears together have drawn much attention these years [18]-[29], e.g., a 12/26/22 outer stator pole / iron piece / inner PM pole-pair counterpart shown in Fig. 1, due to low speed high torque characteristic. MG machines can be potentially applied to electric vehicles (EVs) [21], hybrid electric vehicles (HEVs) [22], and wind turbines [23], [24], as well as high performance motion control applications [25]. For the magnetic gear with two rotating PM bodies whilst the iron pieces are static as analyzed in [14] and [15], the MG machine analyzed in [18] can be obtained by displacing one rotating PM body using an equivalent armature winding stator, as shown in Fig. 1.

For the other category PM machines, *i.e.* stator-PM machines, they also operate based on the magnetic gearing effect, similar to magnetic gears [14]-[17] and MG machines [18]-[29]. The modulation of the salient rotor to the static open-circuit PM field and the rotating armature reaction field makes them synchronous to each other in the air-gap, generating average electromagnetic torque [8]. There are three types of stator-PM machines, including doubly salient PM (DSPM) machines having yoke-inserted PMs [30], [31], switched flux PM (SFPM) machines having tooth-sandwiched PMs [32]-[39] and flux reversal PM (FRPM) machines having tooth-surface-mounted PMs [40]-[42]. Compared with the DSPM and SFPM machines, the FRPM machines have an integral stator lamination, which is better

for manufacturing.

Based on the operation principle of conventional stator-PM machines having single stator, PMs and armature windings in the conventional FRPM machine are separately placed in two stators to form the partitioned stator (PS) FRPM (PS-FRPM) machine with enlarged total stator areas and hence torque density [43], *e.g.* 12/10-stator/rotor-pole PS-FRPM machine shown in Fig. 2. As shown in Fig. 2, the topology of the PS-FRPM machine is similar to the MG machine illustrated in Fig. 1. Indeed, the PS-FRPM machine also operate based on the modulation effect of iron pieces to open-circuit PM and armature reaction MMFs, similar to the PS-SFPM machine. The modulation of the iron pieces to the open-circuit PM and armature reaction fields makes them synchronous in the air-gaps, generating average electromagnetic torque, similar to the MG machine shown in Fig. 1. Similar to a magnetic gear, the armature reaction pole-pair number p_{ar}, the iron piece number N_{ip} and PM pole-pair number p_{PM} in both machines satisfy,
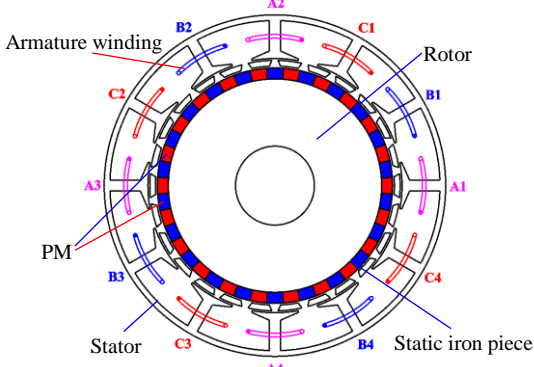
$$N_{ip} = p_{ar} + p_{PM} \qquad (1)$$

Fig. 1. Cross-section of the MG machine having 12/26/22 outer stator pole / iron piece / inner PM pole-pair.
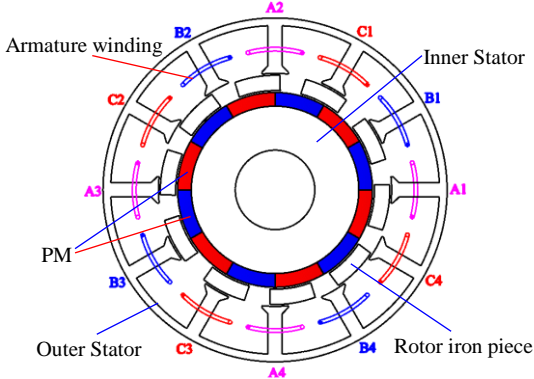

Fig. 2. Cross-section of the PS-FRPM machine having 12/10/6 outer stator pole / iron piece / inner PM pole-pair.

However, two major differences between the PS-FRPM machine shown in Fig. 2 and the conventional MG machine shown in Fig. 1 are,

(1) In the PS-FRPM machine shown in Fig. 2, the PMs are static whilst the iron pieces are rotating. However, the PMs are rotating in the MG machine illustrated in Fig. 1, whilst the iron pieces are static.

(2) Although both the PS-FRPM machine shown in Fig. 2 and the MG machine shown in Fig. 1 have the same outer stator pole number N_{os}=12, the same winding topology and hence the armature reaction pole-pair number p_{ar}=4, [8], the iron piece number N_{ip} and the PM pole-pair number p_{PM} are quite different, i.e. different gear ratios. Similar to the conventional FRPM machines, N_{os}=$2p_{PM}$ in the PS-FRPM machine, and N_{ip}=N_{os} ±2 or N_{ip}=N_{os} ±1.

However, in the conventional MG machines, N_{ip} and p_{PM} are several times of p_{ar}. Therefore, the gear ratio of the conventional MG machine is higher than that of the PS-FRPM machine.

Based on the aforementioned two differences, electromagnetic performance of the conventional MG machine shown in Fig. 1, and the PS-FRPM machine shown in Fig. 2 operating in both SPM and RPM modes will be comprehensively compared in this paper, which aims to provide design guides for a MG machine regarding: (a) a SPM or RPM type machine and (b) a higher or smaller gear ratio machine.

This paper is organized as follows. In section II, the magnetic gearing effect of the conventional MG machine and the PS-FRPM machine operating in both SPM and RPM modes is introduced from the perspective of modulation effect of iron pieces to the open-circuit PM and armature reaction MMFs by a simple MMF-permeance model. This aims to show that the MG machines and the PS-FRPM machines have similar operation principle, i.e. modulation effect, via the qualitative analysis on the pole-pair numbers and rotating speeds of the air-gap field harmonics. The contribution of the main air-gaps harmonics to the average electromagnetic torque is also comparatively investigated for both the conventional MG machine and the PS-FRPM machine in section II. Quantitative and comprehensive comparison of electromagnetic performance of the MG machine and the PS-FRPM machine operating in both SPM and RPM modes is conducted by finite element (FE) analyses in section III. This aims to make recommendations for various applications according to specific requirements, such as lower back-EMF harmonics, cogging torque and torque ripple for wind turbines and motion control applications, and higher power factor for EVs and HEVs. In section IV, the MG machine operating in RPM mode is built and tested to verify the FE predicted results, comparing to the PS-FRPM machine operating in SPM mode which is built and tested in [43].

II. OPERATION PRINCIPLE

In this section, firstly the magnetic gearing effect in the conventional MG machine and the PS-FRPM machine operating in both SPM and RPM modes is introduced based on a simple MMF-permeance model. Then, the contribution of main air-gap field harmonics to the average electromagnetic torque in both PS-FRPM and MG machines is analyzed, as given as follows.

The air-gap permeance waveform accounting for slots between iron pieces is shown in Fig. 3, where $2P_{ip}$ is the peak-to-peak value of air-gap permeance waveform. N_{ip} is the iron piece number. θ_2 is half of the rotor iron piece arc. α_{ip0} is the initial iron piece position. Ω_{ip} is the mechanical angular speed of iron pieces in unit of rad/s, of which the positive direction is anticlockwise. In RPM machines, Ω_{ip}=0. The air-gap permeance waveform can be expressed in Fourier series by,

$$P(\theta, t) = P_0 + \sum_{k=1}^{\infty} \left\{ C_{ipk} \cos \left\{ \frac{k\pi[\theta - (\Omega_{ip}t + \alpha_{ip0})]}{\pi/N_{ip}} \right\} \right\} \quad (2)$$

where P_0 is the DC component of air-gap permeance. C_{ipk} is the Fourier coefficient of the air-gap permeance, which can

be given by,

$$C_{ipk} = \frac{N_{ip}}{\pi} \int_{-\frac{\pi}{N_{ip}}}^{\frac{\pi}{N_{ip}}} P(\theta + \Omega_{ip}t + \alpha_{ip0}, t) \cos\frac{k\pi\theta}{\pi/N_{ip}} d\theta \quad (3)$$
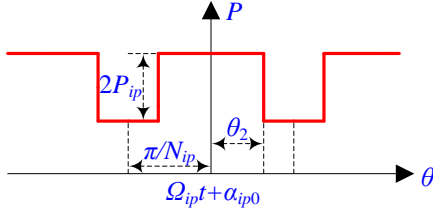$$= \frac{4P_{ip}}{k\pi} \sin(kN_{ip}\theta_2)$$

Fig. 3. Air-gap permeance waveform accounting for slots between iron pieces.

Based on (2) and (3), the Fourier series of the air-gap permeance waveform can be rewritten as,

$$\begin{cases} P(\theta, t) = P_0 + V_{ip} \sum_{k=1}^{\infty} \{M_{ipk} \cos[kN_{ip}(\theta - \Omega_{ip}t - \alpha_{ip0})]\} \\ V_{ip} = \frac{4P_{ip}}{\pi} \\ M_{ipk} = \frac{\sin(kN_{ip}\theta_2)}{k} \end{cases} \quad (4)$$

where V_{ip} is the constant in air-gap permeance. M_{ipk} is the coefficient of air-gap permeance determined by k.

The open-circuit PM MMF is shown in Fig. 4, where p_{PM} is the PM pole-pair number. F_{PMs} is the PM MMF square waveform peak value. θ_1 is the half of arc between PMs. α_{ip0} is the PM position. Ω_{PM} is the mechanical angular speed of PMs in unit of rad/s, of which the positive direction is clockwise. In SPM machines, $\Omega_{PM}=0$. The open-circuit PM MMF waveform can be expressed in Fourier series by,

$$F_{PM}(\theta, t) = \sum_{i=1}^{\infty} \left\{ C_{PMi} \sin\left\{ \frac{i\pi[\theta - (\Omega_{PM}t + \alpha_{PM0})]}{\pi/p_{PM}} \right\} \right\} \quad (5)$$

where C_{PMi} is the Fourier coefficient of the PM MMF, which can be given by,

$$\begin{aligned} C_{PMi} &= \frac{p_{PM}}{\pi} \int_{-\frac{\pi}{p_{PM}}}^{\frac{\pi}{p_{PM}}} F_{PM}(\theta + \Omega_{PM}t + \alpha_{PM0}, t) \sin\frac{i\pi\theta}{\pi/p_{PM}} d\theta \\ &= \frac{2F_{PMs}}{i\pi} [\cos(ip_{PM}\theta_1) - \cos(ip_{PM}\theta_1 - i\pi)] \\ &= \begin{cases} \frac{4F_{PMs}}{i\pi} \cos(ip_{PM}\theta_1), i = 1,3,5, \dots \\ 0, i = 2,4,6, \dots \end{cases} \end{aligned} \quad (6)$$

Based on (5) and (6), the Fourier series of the PM MMF waveform can be rewritten as,

$$\begin{cases} F_{PM}(\theta, t) = V_{PM} \sum_{i=1}^{\infty} \{M_{PMi} \sin[(2i-1)p_{PM}(\theta - \Omega_{PM}t - \alpha_{PM0})]\} \\ V_{PM} = \frac{4F_{PMs}}{\pi} \\ M_{PMi} = \frac{\cos[(2i-1)p_{PM}\theta_1]}{2i-1} \end{cases} \quad (7)$$

where V_{PM} is the constant in PM MMF. M_{PMi} is the coefficient of PM MMF waveform determined by i.

The armature reaction MMF waveform is illustrated in Fig. 5, where F_A, F_B, and F_C are the A-, B-, and C-phase armature reaction MMFs, respectively. N_c is the number of coil turns. θ_3 is half of outer stator tooth arc θ_{ost} plus outer stator tooth tip arc θ_{ot}. i_A, i_B, and i_C are the A-, B-, and C-phase currents, respectively, which can be given by,

$$\begin{cases} i_A = \sqrt{2}I_{rms} \sin(\omega_e t) \\ i_B = \sqrt{2}I_{rms} \sin\left(\omega_e t - \frac{2\pi}{3}\right) \\ i_C = \sqrt{2}I_{rms} \sin\left(\omega_e t + \frac{2\pi}{3}\right) \end{cases} \quad (8)$$

where I_{rms} is the phase current RMS value. ω_e is the rotor electrical angular speed in rad/s.
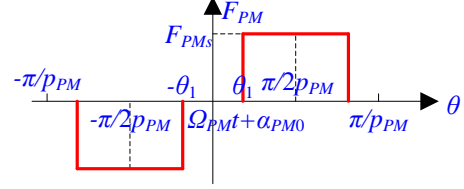

Fig. 4. PM MMF.

The three-phase armature reaction MMF F_{ABC} can be expressed as,

$$F_{ABC}(\theta, t) = F_A(\theta, t) + F_B(\theta, t) + F_C(\theta, t) \quad (9)$$

where $F_A(\theta,t)$, $F_B(\theta,t)$, and $F_C(\theta,t)$ can be expressed in Fourier series by,

$$\begin{cases} F_A(\theta, t) = \frac{N_c i_A}{2} + \sum_{q=1}^{\infty} \left(C_{Aq} \cos\frac{q\pi\theta}{\pi/4} \right) \\ F_B(\theta, t) = \frac{N_c i_B}{2} + \sum_{q=1}^{\infty} \left\{ C_{Bq} \cos\left[\frac{q\pi\left(\theta + \frac{2\pi}{3}\right)}{\pi/4} \right] \right\} \\ F_C(\theta, t) = \frac{N_c i_C}{2} + \sum_{q=1}^{\infty} \left\{ C_{Cq} \cos\left[\frac{q\pi\left(\theta - \frac{2\pi}{3}\right)}{\pi/4} \right] \right\} \end{cases} \quad (10)$$

where C_{Aq}, C_{Bq} and C_{Cq} are the Fourier coefficients of the A-, B-, and C-phase armature reaction MMFs, respectively, which can be given by,

$$\begin{cases} C_{Aq} = \frac{4}{\pi} \int_{-\frac{\pi}{4}}^{\frac{\pi}{4}} F_A(\theta, t) \cos\frac{q\pi\theta}{\pi/4} d\theta \\ C_{Bq} = \frac{4}{\pi} \int_{-\frac{\pi}{4}}^{\frac{\pi}{4}} F_B\left(\theta - \frac{2\pi}{3}, t\right) \cos\frac{q\pi\theta}{\pi/4} d\theta \\ C_{Cq} = \frac{4}{\pi} \int_{-\frac{\pi}{4}}^{\frac{\pi}{4}} F_C\left(\theta + \frac{2\pi}{3}, t\right) \cos\frac{q\pi\theta}{\pi/4} d\theta \end{cases} \quad (11)$$

Based on (8) and Fig. 5, C_{Aq}, C_{Bq} and C_{Cq} shown in (11) can be calculated as,

$$\begin{cases} C_{Aq} = \frac{2\sqrt{2}N_c I_{rms}}{q\pi} \sin(4q\theta_3) \sin(\omega_e t) \\ C_{Bq} = \frac{2\sqrt{2}N_c I_{rms}}{q\pi} \sin(4q\theta_3) \sin\left(\omega_e t - \frac{2\pi}{3}\right) \\ C_{Cq} = \frac{2\sqrt{2}N_c I_{rms}}{q\pi} \sin(4q\theta_3) \sin\left(\omega_e t + \frac{2\pi}{3}\right) \end{cases} \quad (12)$$

Submitting (10) and (12) into (9), the three-phase armature reaction MMF F_{ABC} can be rewritten as,

$$\begin{aligned} F_{ABC}(\theta, t) = \sum_{q=1}^{\infty} \Bigg\{ &\frac{2\sqrt{2}N_c I_{rms}}{q\pi} \sin(4q\theta_3) \Bigg[\left(1 \right. \\ &\left. - \cos\frac{8q\pi}{3}\right) \sin(\omega_e t) \cos(4q\theta) \\ &- \sqrt{3}\sin\frac{8q\pi}{3} \cos(\omega_e t) \sin(4q\theta) \Bigg] \Bigg\} \end{aligned} \quad (13)$$

The three-phase armature reaction MMF F_{ABC} written in

(13) can be simplified as,

$$
\begin{cases}
F_{ABC}(\theta,t) = V_{ABC} \sum_{q=1}^{\infty} [M_{ABCq}\sin(\xi)] \\
V_{ABC} = \dfrac{3\sqrt{2}N_c I_{rms}}{\pi} \\
M_{ABCq} = \dfrac{1}{q}\sin(4q\theta_3) \\
\xi = \begin{cases} -4q\theta + \omega_e t, & q = 3r-2 \\ 4q\theta + \omega_e t, & q = 3r-1 \\ 0, & q = 3r \end{cases}
\end{cases}
\tag{14}
$$

where V_{ABC} is a constant in armature reaction MMF. M_{ABCq} is the coefficient of armature reaction MMF waveform determined by q. r is a positive integer mathematically.
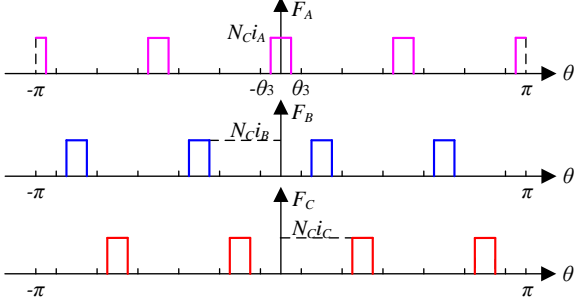

Fig. 5. Armature reaction MMF ($i_A=i_B=i_C$).

Based on (4) and (7), the air-gap open-circuit PM fields can be calculated by,

$$
\begin{aligned}
B_{PM}(\theta,t) &= F_{PM}(\theta,t)P(\theta,t) \\
&= P_0 V_{PM} \sum_{i=1}^{\infty} (M_{PMi}\cos\alpha_1) \\
&\quad + \frac{V_{PM}V_{ip}}{2} \sum_{i=1}^{\infty}\sum_{k=1}^{\infty} [M_{PMi}M_{ipk}(\cos\alpha_2 + \cos\alpha_3)]
\end{aligned}
\tag{15}
$$

where α_j (j=1,2,3) is given by,

$$
\alpha_j = H_j\left(\theta - \frac{\omega_j t + \beta_j}{H_j}\right)
\tag{16}
$$

where H_j, ω_j and β_j/H_j are harmonics order, electric rotating speed and initial phases of air-gap field harmonics. They are given by,

$$
\begin{cases}
H_1 = (2i-1)p_{PM} \\
H_2 = kN_{ip} + (2i-1)p_{PM} \\
H_3 = kN_{ip} - (2i-1)p_{PM}
\end{cases}
\tag{17}
$$

and,

$$
\begin{cases}
\omega_1 = (2i-1)p_{PM}\Omega_{PM} \\
\omega_2 = kN_{ip}\Omega_{ip} + (2i-1)p_{PM}\Omega_{PM} \\
\omega_3 = kN_{ip}\Omega_{ip} - (2i-1)p_{PM}\Omega_{PM}
\end{cases}
\tag{18}
$$

and,

$$
\begin{cases}
\beta_1 = (2i-1)p_{PM}\left(\alpha_{PM0} + \dfrac{\pi}{2}\right) \\
\beta_2 = kN_{ip}\alpha_{ip0} + (2i-1)p_{PM}\alpha_{PM0} + \dfrac{\pi}{2} \\
\beta_3 = kN_{ip}\alpha_{ip0} - (2i-1)p_{PM}\alpha_{PM0} - \dfrac{\pi}{2}
\end{cases}
\tag{19}
$$

respectively.

Similarly, the air-gap armature reaction fields $B_{ABC}(\theta, t)$ can be calculated from (4) and (14), as shown in (20) and (21) when q=3r-2. When q=3r-1, B_{ABC} can also be expressed by them with the coefficient of q multiplied by '-1'.
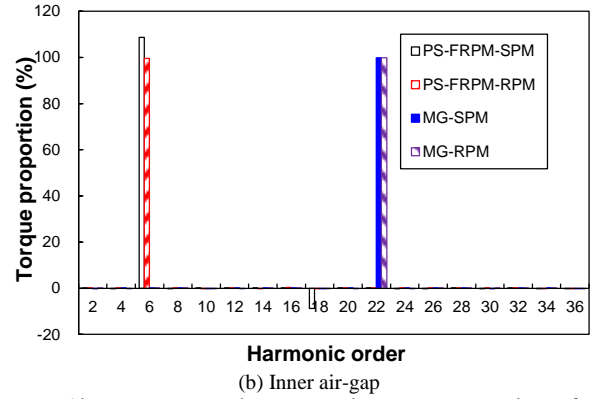
$$
\begin{aligned}
B_{ABC}(\theta,t) &= F_{ABC}(\theta,t)P(\theta,t) \\
&= \frac{3P_0 V_{ABC}}{2}\sum_{q=1}^{\infty}\left\{M_{ABCq}\cos\left[4q\theta - \omega_e t + \frac{\pi}{2}\right]\right\} \\
&\quad + \frac{3V_{ABC}V_2}{4}\sum_{q=1}^{\infty}\sum_{k=1}^{\infty}[M_{ABCq}M_{ipk}(\cos\sigma_1 + \cos\sigma_2)]
\end{aligned}
\tag{20}
$$

where σ_1 and σ_2 are given as,

$$
\begin{cases}
\sigma_1 = (kN_{ip}-4q)\left[\theta - \dfrac{(k-1)\omega_e t + kN_{ip}\theta_0 + \dfrac{\pi}{2}}{kN_{ip}-4q}\right] \\
\sigma_2 = (kN_{ip}+4q)\left[\theta - \dfrac{(k+1)\omega_e t + kN_{ip}\theta_0 - \dfrac{\pi}{2}}{kN_{ip}+4q}\right]
\end{cases}
\tag{21}
$$
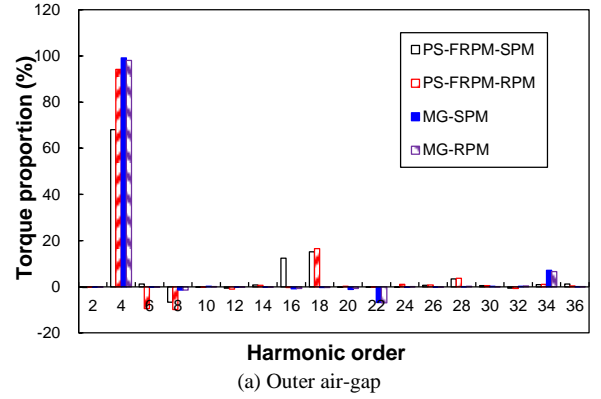
(a) Outer air-gap

(b) Inner air-gap

Fig. 6. Air-gap average electromagnetic torque proportion of main harmonics.

TABLE I

CHARACTERISTICS OF AIR-GAP OPEN-CIRCUIT PM FLUX-DENSITY HARMONICS (i=1,2,3,…)

Pole-Pairs	Electric Rotating Speed (rad/s)
$(2i-1)p_{PM}$	$(2i-1)p_{PM}\Omega_{PM}$
$kN_{ip}+(2i-1)p_{PM}$	$kN_{ip}\Omega_{ip}+(2i-1)p_{PM}\Omega_{PM}$
$|kN_{ip}-(2i-1)p_{PM}|$	$kN_{ip}\Omega_{ip}-(2i-1)p_{PM}\Omega_{PM}$

TABLE II

CHARACTERISTICS OF AIR-GAP ARMATURE REACTION FLUX DENSITY HARMONICS (r=1,2,3,…)

q	Pole-Pairs	Electric Rotating Speed (rad/s)
3r-2	$4q$	$\dfrac{\omega_e}{4q}$
	$|kN_r-4q|$	$\dfrac{k-1}{kN_r-4q}\omega_e$
	kN_r+4q	$\dfrac{k+1}{kN_r+4q}\omega_e$
3r-1	$4q$	$-\dfrac{\omega_e}{4q}$
	kN_r+4q	$\dfrac{k-1}{kN_r+4q}\omega_e$
	$|kN_r-4q|$	$\dfrac{k+1}{kN_r-4q}\omega_e$

TABLE III
CONTRIBUTION OF MAIN AIR-GAP FIELD HARMONICS TO AVERAGE ELECTROMAGNETIC TORQUE IN PS-FRPM MACHINES (%)

Harmonic Order		SPM		RPM	
		Outer	Inner	Outer	Inner
p_{PM}	6	1.17	108.71	-9.44	99.60
N_{ip}-p_{PM}	4	68.03	-0.03	94.13	0.01
N_{ip}+p_{PM}	16	12.36	0.03	-0.29	0.31
$3p_{PM}$	18	15.15	-8.71	16.55	-0.17
$|N_{ip}$-$3p_{PM}|$	8	-6.73	-0.01	-9.89	0.00
N_{ip}+$3p_{PM}$	28	3.44	0.01	3.63	0.07
N_{os}+p_{PM}	18	-	-	-	-
$|N_{os}$-$p_{PM}|$	6	-	-	-	-
SUM	-	93.42	~100	94.69	99.82

TABLE IV
CONTRIBUTION OF MAIN AIR-GAP FIELD HARMONICS TO AVERAGE ELECTROMAGNETIC TORQUE IN MG MACHINES (%)

Harmonic Order		SPM		RPM	
		Outer	Inner	Outer	Inner
p_{PM}	22	-6.87	99.85	-6.98	99.83
N_{ip}-p_{PM}	4	99.17	0.01	98.04	-0.04
N_{ip}+p_{PM}	48	-1.53	0.00	-1.92	0.04
$3p_{PM}$	66	0.03	-0.01	0.01	0.02
$|N_{ip}$-$3p_{PM}|$	40	0.47	0.00	0.59	-0.00
N_{ip}+$3p_{PM}$	92	-0.03	-0.00	-0.06	-0.00
N_{os}+p_{PM}	34	7.06	0.07	6.59	0.08
$|N_{os}$-$p_{PM}|$	10	0.20	-0.05	0.12	-0.05
SUM	-	98.51	99.87	96.39	99.88

TABLE V
OUTER AND INNER AIR-GAP AVERAGE ELECTROMAGNETIC TORQUES (Nm)

Air-gap	PS-FRPM		MG	
	SPM	RPM	SPM	RPM
Outer	1.50	1.01	0.43	0.43
Inner	1.32	1.52	2.34	2.34

Based on the foregoing analytically deduced open-circuit and armature reaction air-gap fields shown in (15) and (20), pole-pairs and electric rotating speed of the open-circuit and armature reaction air-gap fields harmonics can be listed as TABLE I and TABLE II, respectively. Since the open-circuit air-gap fields harmonics listed in TABLE I synchronous with those of armature reaction listed in TABLE II due to the modulation of iron pieces, electromagnetic torque can be generated in both outer and inner air-gaps in both PS-FRPM and MG machines, based on magnetic gearing theory [8]. This can be evidenced by FE predicted air-gap average electromagnetic torque proportion of main harmonics, as shown in Fig. 6, TABLE III and TABLE IV. In Fig. 6(a), the base torque of each machine is the outer air-gap average torque shown in TABLE V, respectively. Similarly, the base torque of each machine in Fig. 6(b) is the inner air-gap average torque shown in TABLE V, respectively.

As listed in TABLE III and TABLE IV, in all the four analyzed PS-FRPM and MG machines operating in both SPM and RPM modes, more than 93% of the average electromagnetic torque is contributed by several dominant air-gap filed harmonics, *i.e.* those having pole-pairs of $(2i-1)p_{PM}$ (i=1, 2), $|kN_{ip}\pm(2i-1)p_{PM}|$ (k=1, i=1), and $|N_{os}\pm(2i-1)p_{PM}|$. This is different from the conventional magnetic gear [15], in which the average electromagnetic torque is generated by two dominant air-gap filed harmonics having pole-pairs of outer and inner PM pole-pairs. It is worth noting that the air-gap filed harmonics having pole-pairs of $|N_{os}\pm(2i-1)p_{PM}|$ are due to the modulation of the outer stator slots to the open-circuit PM and armature reaction MMFs, similar to vernier machines [13].

Similar to magnetic gears [15], different gear ratios can be achieved in the PS-FRPM machine and the MG machine operating in SPM and RPM modes. For both the PS-FRPM machine and the MG machine, the gear ratios G_r can be respectively given by,

$$G_r = \frac{N_{ip}}{p_{ar}} \tag{22}$$

and,

$$G_r = \frac{p_{PM}}{p_{ar}} \tag{23}$$

for SPM and RPM modes, respectively.

The gear ratios of the PS-FRPM machine and the MG machine operating at SPM and RPM modes are listed in TABLE VI. Generally, the conventional MG machines have higher gear ratios than the PS-FRPM machine due to the larger iron piece number and PM pole-pair number. Also, the SPM machines have slightly higher gear ratios than their RPM counterparts since the iron piece number is higher than PM pole-pair number, respectively.

TABLE VI
GEAR RATIOS OF PS-FRPM AND MG MACHINES OPERATING IN SPM AND RPM MODES

Parameters	PS-FRPM		MG	
Operation modes	SPM	RPM	SPM	RPM
Winding body pole number, N_{os}	12			
Armature reaction pole-pair, p_{ar}	4			
Iron piece number, N_{ip}	10		26	
PM pole-pair, p_{PM}	6		22	
Gear ratio, G_r	2.5	1.5	6.5	5.5

III. ELECTROMAGNETIC PERFORMANCE EVALUATION

In the foregoing analysis, it is found that the PS-FRPM machine and the MG machine have the same operation principle, operating based on the modulation effect of iron pieces to the open-circuit PM and armature reaction MMFs.

In this section, the electromagnetic performance of PS-FRPM and MG machines operating in both SPM and RPM modes will be comparatively analyzed, including open-circuit flux distribution, phase flux-linkage and back-EMF, torque characteristics, loss and efficiency, inductance and power factor. Back-EMF is induced by the variation of flux-linkage, which can be integrated by the flux density along the certain path. Flux distribution can also indicate the ratio of the flux-leakage to the main flux, which is corresponding to the power factor. As well known, a low power factor will increase the power rating of the inverter. On-load torque is made up of three parts, i.e. cogging torque, PM torque due to the back-EMF and reluctance torque. Generally, average torque and efficiency are important for all the EVs, HEVs, wind generation and motion control applications. Specifically, a more sinusoidal back-EMF, a lower cogging torque and also a smoother torque are desired for wind turbines [44], as the cogging torque and pulsating torque are harmful to the starting and running of wind turbines, and the motion control applications. However, a higher power factor is also desired for machines applied to EVs and HEVs for reducing the inverter power rating due to the compact space for the inverter [1].

The dimensional parameters of the four analyzed machines are shown in TABLE VII, which can be referred in the linear illustration shown in Fig. 7. Since a higher average torque is commonly desired for all applications, the design parameters of the four analyzed machines are obtained by optimizing for the highest average electromagnetic torque with a fixed copper loss for a fair comparison, i.e. p_{cu}=20W. In TABLE VII, parameters from N_{os} to l_{otbs} in TABLE VII

are fixed for each machine, whilst those from R_{oy} to θ_{ipo} are optimized under zero *d*-axis current control, *i.e.* i_d=0. It should be noted that in the optimization the PM volume is fixed as 13414.6mm³, similar to the PS-FRPM-SPM machine in [43].

As foregoing mentioned, both a higher average torque and a larger efficiency are desired for any application. With a fixed copper loss and much smaller iron loss and PM eddy current loss, the design with a larger average torque also features a higher efficiency approximately. Therefore, by optimizing the machine for the largest average torque with a fixed copper loss, a high efficiency can also be obtained.

TABLE VII
PARAMETERS OF PS-FRPM AND MG MACHINES

Parameters	Unit	PS-FRPM		MG	
Operation modes	-	SPM	RPM	SPM	RPM
Stack length, L_s	mm	25			
Outer stator outer radius, R_{oo}	mm	45			
PM body inner radius, R_{ii}	mm	10.4			
Outer air-gap width, g_o	mm	0.5			
Inner air-gap width, g_i	mm	0.5			
Winding body tooth tip top length, l_{ott}	mm	0.5			
Winding body tip bottom length, l_{otb}	mm	2			
Winding body yoke radius, R_{oy}	mm	43	42.5	43.5	43.5
Winding body inner radius, R_{oi}	mm	31	32	34	33.5
Iron piece inner edge radius, R_{ipi}	mm	26.5	27	32	31.5
Winding body tooth arc, θ_{ot}	°	7	9	5	5
Winding body tooth tip arc, θ_{otip}	°	3	4	8	8
Iron piece outer edge arc, θ_{ipo}	°	23	23	11	11
Iron piece inner edge arc, θ_{ipi}	°	24	26.5	8.5	8.5
PM remanence, B_r	T	1.2			
PM relative permeability, μ_r	-	1.05			
PM bulk conductivity, κ_{PM}	s/m	625000			
Slot packing factor, k_{pf}	-	0.5			
Phase RMS ampere turns at p_{cu}=20W, AT_{rms}	A	1180.8	1056.4	1078.9	1110.7

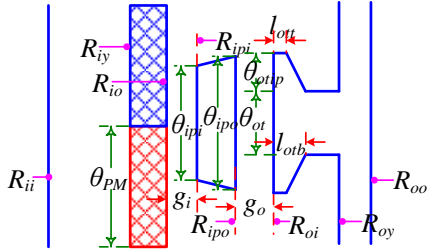

Fig. 7. Illustration of design parameters in PS-FRPM and MG machines.

The reason why p_{cu}=20W is selected as a reference for a fair comparison of the four analyzed machines in this paper is explained as follows. As well known, the same thermal condition is usually required for a fair comparison in different machines. When the mechanical loss is neglected, the copper loss, iron loss, and PM eddy current loss are the main thermal sources. Due to the low rotor speed, the copper loss is much higher than both the iron loss and the PM eddy current loss, as will be shown later. Therefore, the same copper loss is applied in the comparison since the PS-FRPM and MG machines having similar topology, similar operation principle, and also same outer radius and stack length. The value of the copper loss 20W is determined to make sure a machine having stack length L_s=25mm and outer radius R_o=45mm of which the average electromagnetic torque T_{avg}=2Nm has an efficiency over 80% at 400rpm. However, a higher copper loss will make challenges to the thermal dissipation.
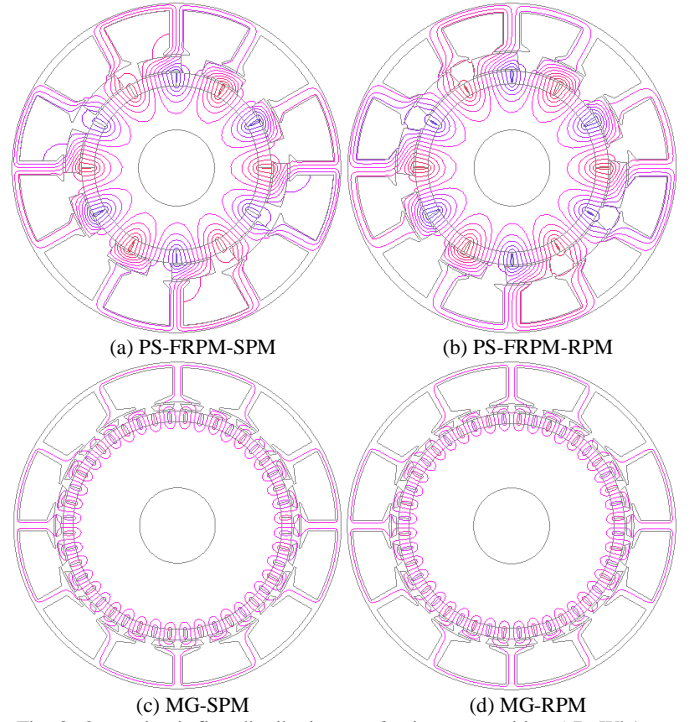

(a) PS-FRPM-SPM   (b) PS-FRPM-RPM

(c) MG-SPM   (d) MG-RPM

Fig. 8. Open-circuit flux distributions at *d*-axis rotor position (-7mWb/m ~ 7mWb/m).
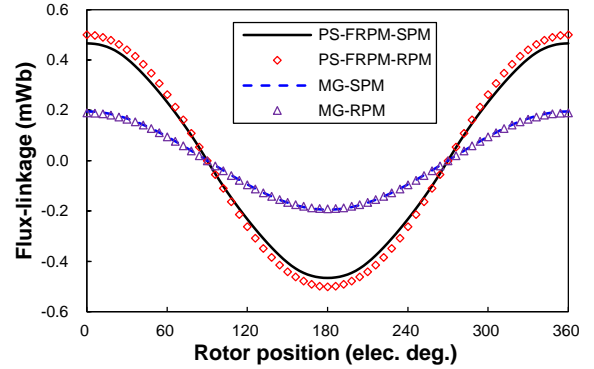

Fig. 9. Open-circuit phase A flux-linkage waveforms (coil number turns N_c=1).

A. Open-Circuit Flux-Linkage, Back-EMF, and cogging torque

Fig. 8 illustrates the open-circuit flux distribution at *d*-axis rotor position. Compared with the PS-FRPM machines, the MG machines suffer from more severe flux-leakage between iron pieces and PMs, which do not cross armature teeth. This is due to the higher gear ratios with higher iron piece number or PM pole-pair number. As a consequence, the MG-SPM and MG-RPM machines have lower phase flux-linkages, as shown in Fig. 9.
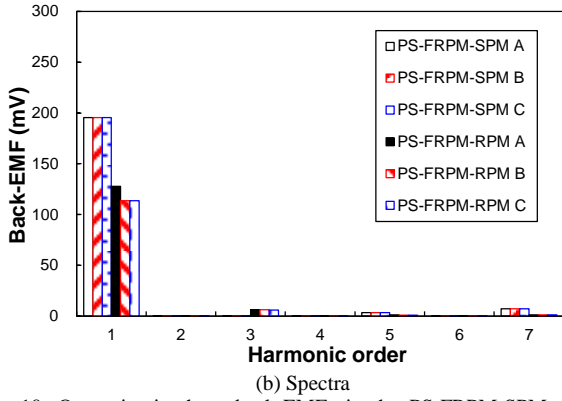

(a) Waveforms

(b) Spectra
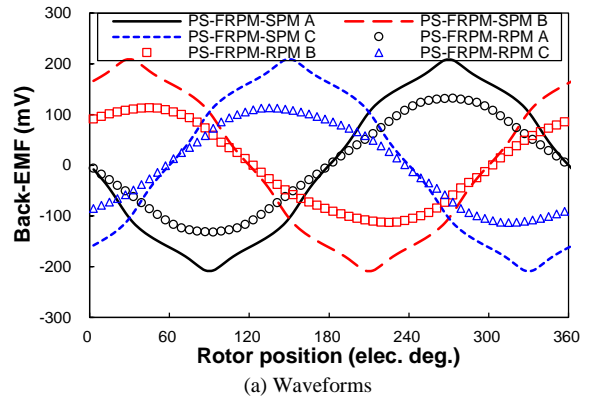
Fig. 10. Open-circuit phase back-EMFs in the PS-FRPM-SPM and PS-FRPM-RPM machines (N_c=1, 400rpm).

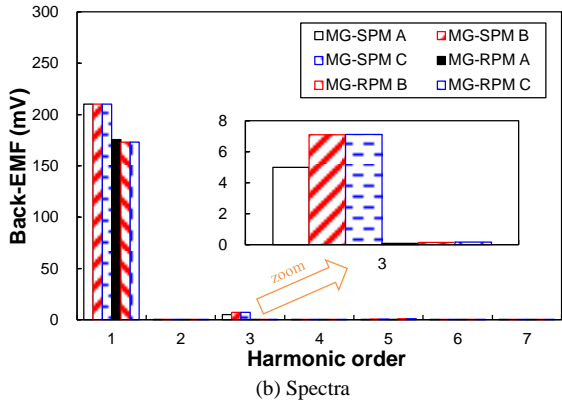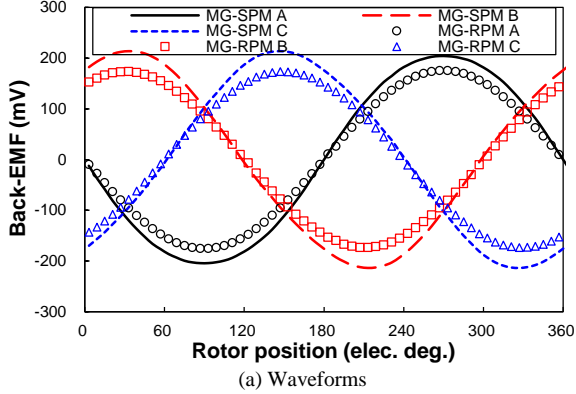(a) Waveforms

(b) Spectra

Fig. 11. Open-circuit phase back-EMFs in the MG-SPM and MG-RPM machines (N_c=1, 400rpm).

However, due to higher gear ratios with higher iron piece number or PM pole-pair number, the MG-SPM and MG-RPM machines exhibit larger fundamental phase back-EMFs than the PS-FRPM-SPM and PS-FRPM-RPM machines, respectively, as shown in Fig. 10 and Fig. 11. More importantly, it can be observed that the PS-FRPM-SPM machine has larger fundamental phase back-EMF than the PS-FRPM-RPM machine, although the flux-linkage of the PS-FRPM-SPM machine is even lower. This is due to that the 66.67% higher electric frequency in the PS-FRPM-SPM machine than the PS-FRPM-RPM machine, as $N_{ip}>p_{PM}$. Similar trend can be observed between the MG-SPM and MG-RPM machines. However, the electric frequency in the MG-SPM machine is only 18.2% higher than the MG-RPM machine.
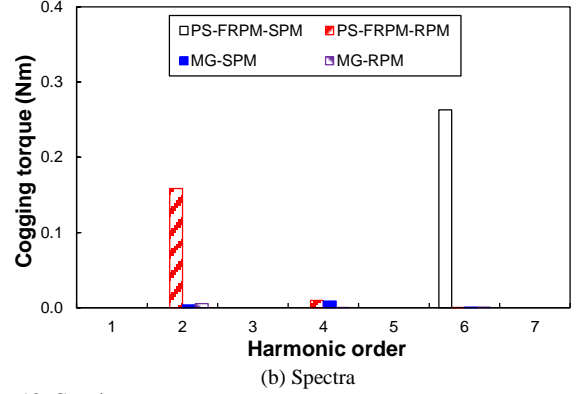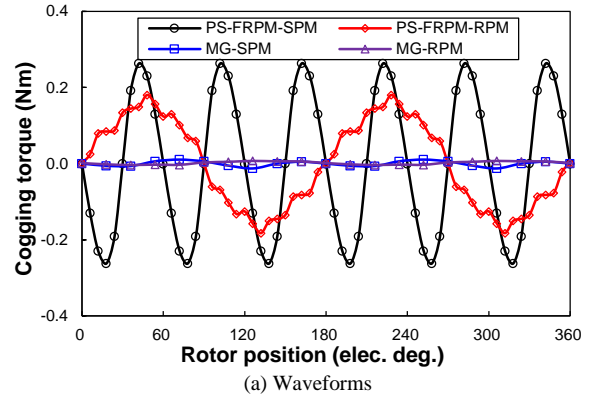

(a) Waveforms

(b) Spectra

Fig. 12. Cogging torque.

TABLE VIII
TORQUE CHARACTERISTICS OF PS-FRPM AND MG MACHINES

Item	Unit	PS-FRPM		MG	
Operation mode	-	SPM	RPM	SPM	RPM
T_{avg}	Nm	0.53	0.36	0.02	0.01
T_{avg}	Nm	2.82	1.52	2.77	2.34
T_{max}	Nm	3.09	1.80	2.91	2.37
T_{min}	Nm	2.56	1.25	2.62	2.30
T_r	%	18.56	35.92	10.43	3.01

As shown in Fig. 10 and Fig. 11, the PS-FRPM-SPM machine has three-phase symmetrical back-EMFs, whilst other three machines suffer from three-phase asymmetric back-EMFs which are caused by the unbalanced magnetic circuits. The PS-FRPM-RPM machine shown in Fig. 8(b) suffers from the highest asymmetry, as evidenced by Fig. 10(b).

Cogging torque in PM machines will cause torque ripple, vibration, and acoustic noise, especially at a low rotor speed. Here, the cogging torques in the four analyzed machines are compared in Fig. 12 and TABLE VIII. In TABLE VIII, T_{cog} is defined as the peak to peak value of the cogging torque waveforms shown in Fig. 12. Since the difference between the PM pole-pair number and the iron piece number is higher [5], the PS-FRPM machines suffer from larger T_{cog} than the MG machines.

B. On-Load Torque Characteristics

On-load average electromagnetic torque versus current angle for the four analyzed machines are illustrated in Fig. 13. It can be observed that the reluctance torque of all these four machines are negligible due to similar d- and q-axis inductances L_d and L_q, which will be shown later. Therefore, zero d-axis current control, i.e. i_d=0, is applied to all of them, at brushless AC mode. It is worth noting that in this paper the FE predicted electromagnetic torque is calculated by injecting three-phase symmetrical sinusoidal currents into the three-phase windings.
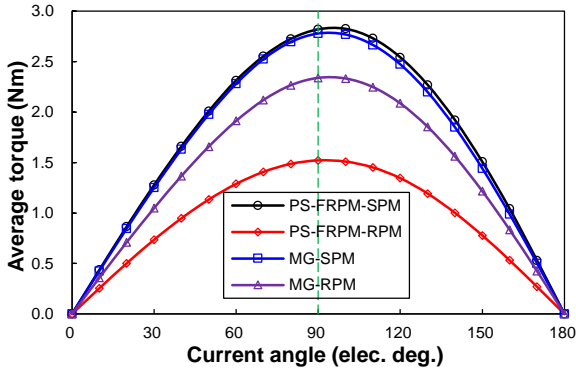
Fig. 13. Average torque versus current angle (BLAC, p_{cu}=20W).

The rated on-load electromagnetic torque waveforms with same copper loss p_{cu}=20W are comparatively shown in Fig. 14, of which the characteristics are listed in TABLE VIII. For the SPM and RPM machines, the average electromagnetic torque T_{avg} can be respectively given by,

$$T_{avg} = \frac{3E_{p1}I_{p1}}{2\Omega_{ip}} = \frac{3}{2}N_{ip}\psi_{p1}I_{p1} \qquad (24)$$

and,

$$T_{avg} = \frac{3E_{p1}I_{p1}}{2\Omega_{PM}} = \frac{3}{2}p_{PM}\psi_{p1}I_{p1} \qquad (25)$$

where E_{p1}, I_{p1}, and ψ_{p1} are phase fundamental back-EMF, phase fundamental current values, and phase fundamental flux-linkage, respectively.

As shown in Fig. 14, the SPM machines generally have higher average electromagnetic torque T_{avg} than their RPM counterparts for both the PS-FRPM and MG machines. This can be explained by (24) and (25), since N_{ip} is higher than p_{PM} as shown in (1) whilst ψ_{p1} and I_{p1} are similar. Therefore, a SPM type machine is recommended to enhance the electric frequency, and hence the back-EMF and torque.

Although the PS-FRPM-SPM machine suffers from 6.98% lower fundamental phase back-EMF than the MG-SPM machine, as shown in Fig. 10, the torque is similar when the copper loss p_{cu}=20W, as shown in Fig. 14 and TABLE VIII. This can also be explained by (24) and (25), as the PS-FRPM-SPM machine has a 19.39% larger half slot area, *i.e.* 76.65mm^2 and 91.51mm^2, and hence electric load than the MG-SPM machine. More importantly, the average torque difference between the PS-FRPM-SPM and MG-SPM machines becomes higher with copper loss, since the MG-SPM having thinner iron pieces is easier to be saturated.

From the perspective of the higher phase fundamental back-EMF and hence average torque for all applications, the SPM machines are preferred, as shown in Fig. 10, Fig. 11, Fig. 14 and Fig. 15.
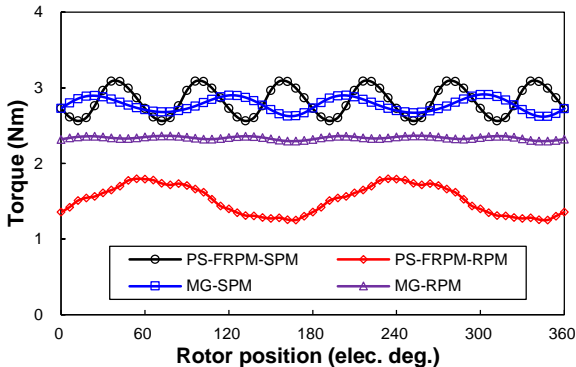
(a) Waveforms
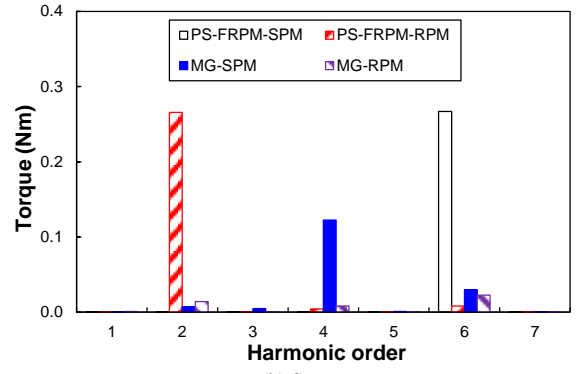
(b) Spectra

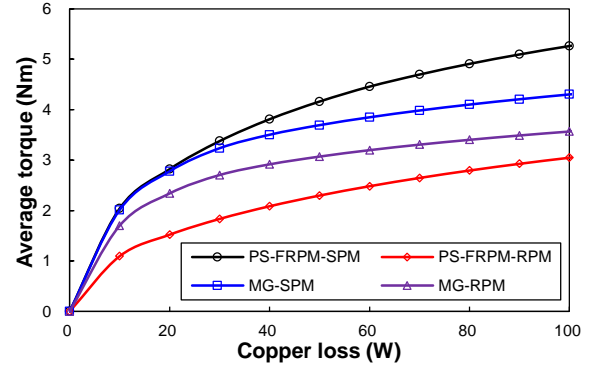Fig. 14. On-load electromagnetic torque (BLAC, i_d=0, p_{cu}=20W).

Fig. 15. Average torque versus copper loss (BLAC, i_d=0).

Besides the average torque, torque ripple is another important torque characteristic in electrical machines especially in those for high performance motion control applications such as direct drive robots [45]. Since the reluctance torques are negligible in the four analyzed machines, Fig. 13, their torque ripples are mainly caused by back-EMF and cogging torque. As for the torque ripple caused by back-EMF, generally, one phase m^{th} (m=1, 2, 3…) back-EMF will generate $(m-1)^{th}$ and $(m+1)^{th}$ torque ripple after interacting with the injected fundamental sinusoidal current. However, if three-phase m^{th} back-EMFs are symmetrical, only the torque ripple harmonics satisfy $m+1$=3n (n=1, 2, 3…) or $m-1$=3n (n=1, 2, 3…) remain since the corresponding three-phase phase angles are same, whilst others are eliminated since the corresponding three-phase phase angles are symmetrical.

As shown in TABLE VIII and Fig. 14, the PS-FRPM-RPM machine suffers from the largest torque ripple with a dominant 2nd harmonic, which is caused by the different three-phase fundamental back-EMFs, as shown in Fig. 10(b). In addition, the high cogging torque of the PS-FRPM-SPM machine shown in Fig. 12 also contributes to the large torque ripple. Although the three-phase back-EMFs are symmetrical, the PS-FRPM-SPM machine also has a higher torque ripple, i.e. 18.56%. This is due to the largest cogging torque in the PS-FRPM-SPM machine, as shown in Fig. 12. Since the cogging torque is low in the MG-SPM and MG-RPM machines, as shown in Fig. 12, their torque ripples are mainly caused by the back-EMFs shown in Fig. 11. The torque ripple in the MG-SPM machine is higher than that of the MG-RPM machine, i.e. 10.43% and 3.01%, respectively. The dominant 4th torque harmonic in the MG-SPM machine is caused by the three-phase asymmetric 3rd back-EMF harmonics, as shown in Fig. 11(b). In TABLE VIII, the torque ripple T_r is defined as,

$$T_r = \frac{T_{max} - T_{min}}{T_{avg}} \times 100\% \qquad (26)$$

where T_{max} and T_{min} are the maximum and minimum electromagnetic torque, respectively.

From the perspective of a more sinusoidal phase back-EMF, a lower cogging torque and a smaller torque ripple, the MG machines are more suitable for wind turbines and motion control applications, as shown in Fig. 10, Fig. 11, Fig. 12 and Fig. 14.

C. Loss and Efficiency

Fig. 16 and Fig. 17 show the iron loss and PM eddy current loss versus rotor speed, respectively. Due to higher gear ratios with higher electric frequencies, the MG-SPM and MG-RPM machines suffer from higher iron loss p_{iron} than the PS-FRPM-SPM and PS-FRPM-RPM machines. However, the PM eddy current loss p_{PMe} of the MG-SPM and MG-RPM machines are smaller than the PS-FRPM-SPM and PS-FRPM-RPM machines. This is due to the smaller PM bulk volume in the MG-SPM and MG-RPM machines having higher PM pole-pair number. However, the PM eddy current loss p_{PMe} is smaller than the iron loss p_{iron}. Therefore, a smaller gear ratio machine is preferred to achieve a smaller electric frequency and hence iron loss, albeit with a slight higher PM eddy current loss.

It is worth noting that, when the rotor speed is 400rpm, both the iron loss p_{iron} and the PM eddy current loss p_{PMe} are much smaller than the copper loss p_{cu}=20W. This is why in the global optimization, the iron loss and PM eddy current loss is not accounted. In Fig. 16, the iron loss p_{iron} is made up of three parts, i.e. hysteresis loss p_{hy}, eddy current loss p_{ed} and excess loss p_{ex},

$$\begin{aligned}p_{iron} &= p_{hy} + p_{ed} + p_{ex} \\ &= k_{hy}f B_m^2 + k_{ed}f^2 B_m^2 + k_{ex}f^{1.5}B_m^{1.5}\end{aligned} \qquad (27)$$

where k_{hy}, k_{ed} and k_{ex} are the hysteresis, eddy current and excess loss coefficients, respectively. They are k_{hy}=261.64W/m^3, k_{ed}=0.10037W/m^3, and k_{ex}=3.296W/m^3, respectively. B_m is the maximum flux density.
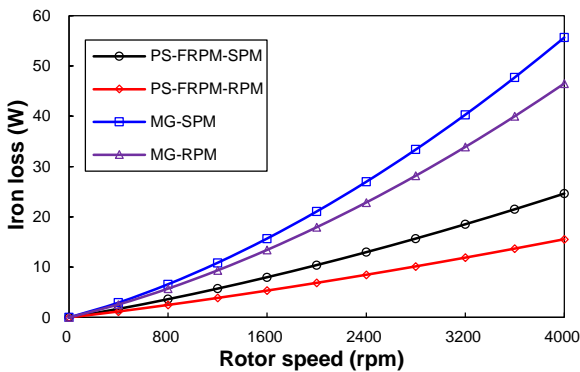

Fig. 16. Iron loss versus rotor speed.

TABLE IX lists torque, loss, efficiency characteristics of the four analyzed machines at 400rpm. Generally, the SPM machines can exhibit higher torque and efficiency than the RPM machines, in spite of slightly larger iron loss due to higher electric frequency. The power density of the PS-FRPM-SPM and MG-SPM machines can reach 732665 and 712025 W/m^3, respectively. In TABLE IX, T_{avg} and P_{avg} are the average electromagnetic torque and power, respectively, whilst P_{out} and T_{out} are the average output torque and power, respectively, and V is the machine volume. It is worth noting that the efficiency η in TABLE IX is calculated by the percentage of the output power P_{out} to the input power P_{in},

$$\eta = \frac{P_{out}}{P_{in}} \times 100\% = \frac{P_{avg} - p_{iron} - p_{PMe}}{P_{avg} + p_{cu}} \times 100\% \qquad (28)$$
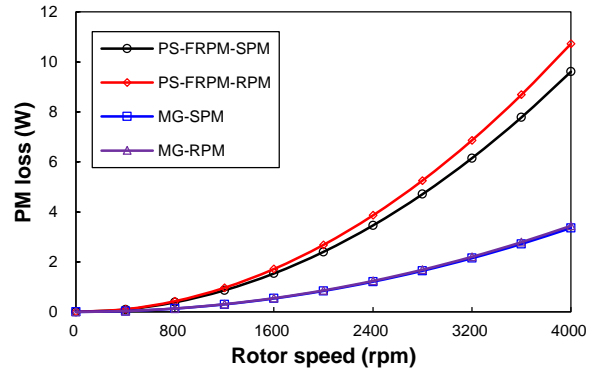

Fig. 17. PM eddy current loss versus rotor speed.

TABLE IX
TORQUE, LOSS, EFFICIENCY CHARACTERISTICS OF PS-FRPM AND MG MACHINES AT 400RPM

Item	Unit	PS-FRPM		MG	
Operation mode	-	SPM	RPM	SPM	RPM
T_{avg}	Nm	2.82	1.52	2.77	2.34
P_{avg}	W	118.3	63.6	116.2	98.0
p_{iron}	W	1.7	1.2	2.9	2.6
p_{PMe}	W	0.096	0.107	0.034	0.034
P_{out}	W	116.5	62.3	113.2	95.4
T_{out}	Nm	2.78	1.49	2.70	2.28
V	mm^3	159043			
P_{out}/V	W/m^3	732665	391960	712025	599587
T_{out}/V	Nm/m^3	17491	9357	16998	14314
p_{cu}	W	20			
P_{in}	W	138.3	83.6	136.2	118.0
η	%	84.24	74.53	83.13	80.83

D. Winding Inductance and Power Factor

TABLE X lists self-inductance and mutual-inductance of the four analyzed machines. They have similar mutual-inductance, whilst the PS-FRPM-SPM machine has smaller self-inductance than the others three machines, as well as d- and q-axis inductances. As shown in TABLE X, in all the four analyzed machines, d- and q-axis inductances are similar and hence the reluctance torques are negligible, as shown in Fig. 13. This is due to the d- and q-axis similar magnetic paths via iron pieces and inner PM body.

TABLE X
INDUCTANCES PS-FRPM AND MG MACHINES

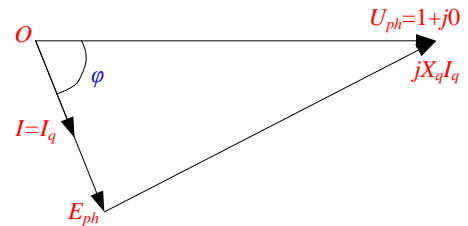| Item	Unit	PS-FRPM		MG	
Operation mode	mH	SPM	RPM	SPM	RPM
Self-inductance, L_{AA}	mH	0.17	0.21	0.22	0.23
Mutual-inductance, M_{BA}	mH	-0.08	-0.09	-0.10	-0.10
Mutual-inductance, M_{CA}	mH	-0.08	-0.09	-0.10	-0.10
d-axis inductance, L_d	mH	0.23	0.30	0.33	0.33
q-axis inductance, L_q	mH	0.26	0.30	0.32	0.33

Fig. 18. Phasor diagram with i_d=0.

Based on the phasor diagram shown in Fig. 18 in which phase resistance voltage drop is neglected, the power factors of the four analyzed machines are listed in TABLE XI as cosine value of the angle φ, i.e. $cos(\varphi)$. In Fig. 18, E_{ph} is the open-circuit phase back-EMF. U_{ph} is the on-load phase

terminal voltage. X_q is the q-axis reactance. I_q is the q-axis current. All of these parameters are in per unit (p.u.) value. As listed in TABLE XI, the PS-FRPM-SPM machine has similar power factor as its RPM counterpart, and the MG-SPM and MG-RPM machines have similar power factor as well. However, due to higher gear ratios with higher electric frequencies, both MG-SPM and MG-RPM machines suffer from lower power factor. This makes challenges to the inverter power rating. Therefore, from the perspective of a smaller inverter power rating, the PS-FRPM machines are recommended for the EVs and HEVs, since they feature higher power factors, as shown in TABLE XI.

TABLE XI
SYNCHRONOUS REACTANCE AND POWER FACTOR OF PS-FRPM AND MG MACHINES AT 400RPM

Item	PS-FRPM		MG	
Operation mode	SPM	RPM	SPM	RPM
Synchronous reactance	0.58	0.62	0.90	0.90
Power factor	0.81	0.78	0.45	0.43

IV. EXPERIMENTAL VALIDATION

In the foregoing analysis, electromagnetic performance of the PS-FRPM machine and the conventional MG machine operating in both SPM and RPM modes are comprehensively compared by FE analyses. FE results show that the PS-FRPM machine operating in SPM mode exhibits higher torque, efficiency, and power factor than its RPM counterpart. The experiment results of the PS-FRPM-SPM prototype machine have been reported in [43] in terms of phase back-EMF waveforms and static torques. Here, the MG-RPM machine is built and the phase back-EMF, static torque, and winding inductances including both self- and mutual-inductances are tested. These measured results will be presented together with comparison to those of the PS-FRPM-SPM prototype to verify the FE predicted results.

Fig. 19 and Fig. 20 show the pictures of the two prototypes, respectively. Both prototypes are wound with number of turns per phase N_{ph}=72. It is worth noting that to ease manufacturing, the PM thickness is modified to 4mm in both machines. Also, for easier assembling the rotor iron pieces, an iron bridge of thickness 0.5mm is introduced adjacent to the inner air-gap to connected iron pieces in both prototypes.
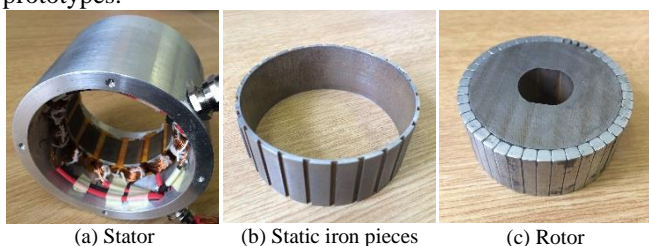

(a) Stator　　　　(b) Static iron pieces　　　　(c) Rotor
Fig. 19. Photos of MG-RPM prototype machine.

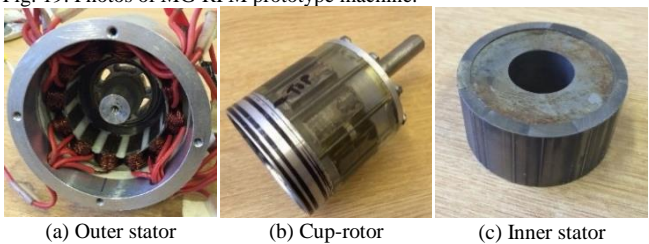(a) Outer stator　　　(b) Cup-rotor　　　(c) Inner stator
Fig. 20. Photos of PS-FRPM-SPM prototype machine.

Fig. 21 shows the comparison of the measured and 2D FE predicted phase back-EMFs, from which it can be observed that 2D FE predicted values are slightly lower than the measured ones due to end effect in both machines. As shown

in Fig. 21, the measured phase back-EMF of the PS-FRPM-SPM prototype is more than twice of that of the MG-RPM prototype. It is worth noting that the phase fundamental back-EMF dropped 53.83% in the MG-RPM machine, due to the introduction of the 0.5mm iron bridge for the static iron pieces which is one third of the total thickness of iron pieces, $i.e.$ 1.5mm.
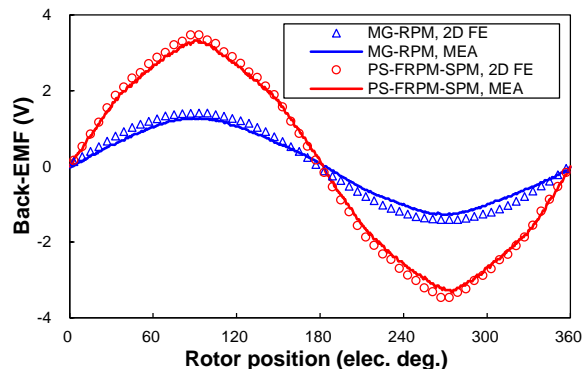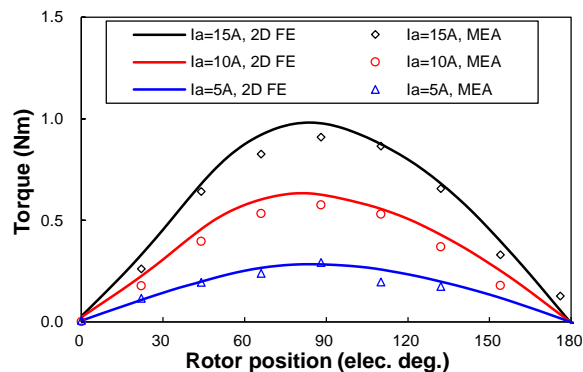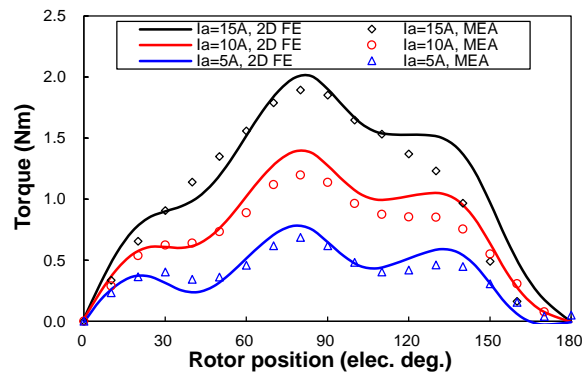

(a) Waveforms
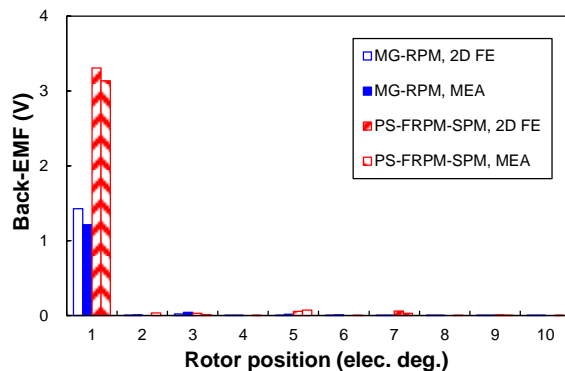
(b) Spectra
Fig. 21. Comparison of measured and 2D FE predicted phase back-EMFs in MG-RPM and PS-FRPM-SPM machines at 400rpm.

(a) MG-RPM

(b) PS-FRPM-SPM
Fig. 22. Comparison of measured and 2D FE predicted torque variations with rotor position (I_a= -2I_b= -2I_c).
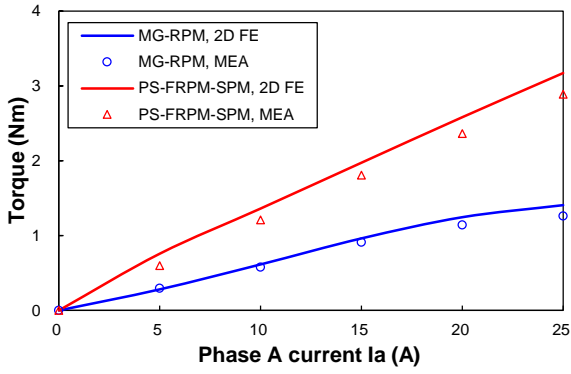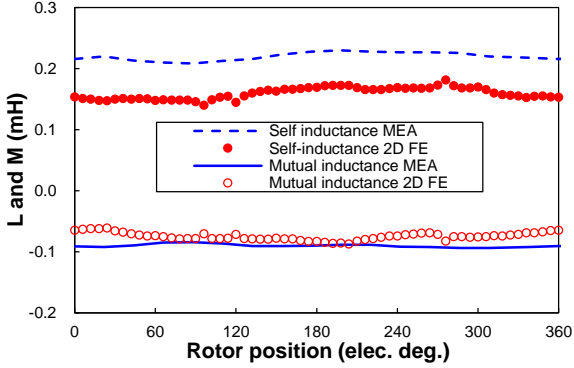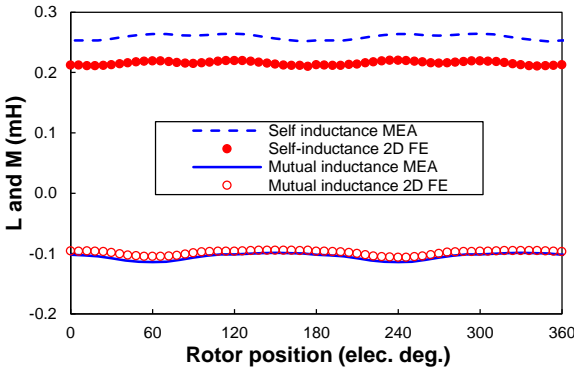
Fig. 23. Comparison of measured and 2D FE predicted peak static torque with phase A current I_a ($I_a = -2I_b = -2I_c$).

(a) MG-RPM

(b) PS-FRPM-SPM

Fig. 24. Comparison of measured and 2D FE predicted self- and mutual-inductances.

The static torques with current angle of the prototype machines are measured based on the test method reported in [46]. Fig. 22 shows the comparison of the measured and 2D FE predicted torque variations with rotor position. As for the peak torque, the comparison between the measured and 2D FE predicted results under different phase A current I_a is shown in Fig. 23. Again, the 2D FE predicted and measured static torques agree well with each other, although the 2D FE predicted results are slightly smaller in both prototypes due to end effect. As shown in Fig. 22 and Fig. 23, the measured static torque of the PS-FRPM-SPM prototype is higher than that of the MG-RPM prototype. Nevertheless, the MG-RPM prototype is easier to be saturated than the PS-FRPM-SPM prototype, as predicted by FE in Fig. 15. It is worth noting that in the measurement of static torque, three-phase currents I_a, I_b, and I_c are set as,

$$I_a = -2I_b = -2I_c \qquad (29)$$

For the winding inductances including both self- and mutual-inductance, the comparison between the 2D FE predicted values and those measured by LCR meter are shown in Fig. 24. It is worth noting that the self-inductance shown in Fig. 24 is directly measured by the Hioki-LCR

meter 3522 at $20°C$, whilst the mutual-inductance between phase A and B, M is calculated by,

$$M = \frac{L_{A+B} - L_A - L_B}{2} \qquad (30)$$

where L_{A+B} is the self-inductance when the windings of phase A and phase B are serially connected. L_A is the self-inductance of phase A winding. L_B is the self-inductance of phase B winding.

As can be observed from Fig. 24, the mutual-inductance predicted by 2D FE and those calculated based on (30) agree well with each other in both prototypes. However, the 2D FE predicted self-inductance is slightly smaller than the measured one. This can be explained as follows. Since the 2D FE predicted self-inductance cannot account for the end winding inductance, it is slightly smaller than that measured by LCR meter [47]. However, this influence can be eliminated based on (30) for the calculation of the mutual-inductance between phase A and B, M_{BA}. Therefore, the 2D FE predicted mutual-inductance and that calculated based on on (30) agree well with each other in both prototypes.

It is worth noting that the FE predicted and measured inductances shown in Fig. 24 are obtained at a low phase current, i.e. 0.1A. The d- and q-axis inductances of both prototypes at rated condition are also tested based on the standstill frequency response method [48]. The d- and q-axis inductances L_d and L_q can be obtained as the values of the inductance L_{A-B}, i.e. the self-inductance when the windings of phase A and phase B are oppositely connected, at d- and q-axis positions, respectively [48]. As shown in Fig. 25, the measured inductance L_{A-B} is slightly higher than the 2D FE predicted values again in both prototypes due to the end winding inductance [47], and hence L_d and L_q shown in TABLE XII.
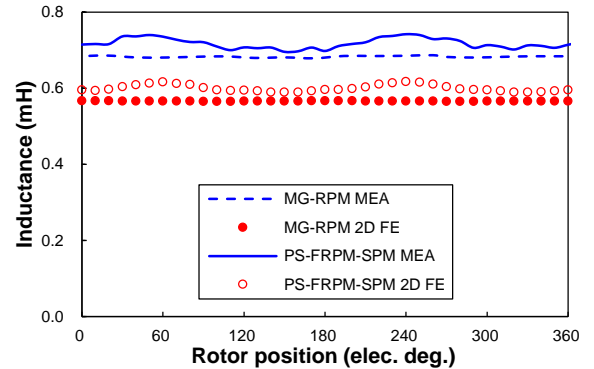

Fig. 25. Comparison of 2D FE predicted and measured inductance L_{A-B}.

TABLE XII
COMPARISON OF MEASURED AND 2D FE PREDICTED D- AND Q-AXIS INDUCTANCES

Item	Unit	MG-RPM	PS-FRPM-SPM
L_d MEA	mH	0.68	0.70
L_d 2D FE	mH	0.56	0.59
L_q MEA	mH	0.69	0.74
L_q 2D FE	mH	0.57	0.62

V. CONCLUSIONS

The PS-FRPM and MG machines operating in SPM and RPM modes are comparatively analyzed in this paper. The comparison results can be summarized as

(1) The PS-FRPM-SPM and PS-FRPM-RPM machines have smaller flux-leakage and hence higher main flux than the MG-SPM and MG-RPM machines, due to the smaller iron piece number and PM pole-pair number.

(2) The PS-FRPM-SPM and MG-SPM machines have higher fundamental back-EMFs than their RPM counterparts, respectively, due to the larger electric frequency since the iron piece number is larger than the PM pole-pair number. The MG-SPM machine has the highest phase fundamental back-EMF, whilst the MG-RPM features the lowest phase back-EMF harmonics.

(3) The MG-SPM and MG-RPM machines have much smaller cogging torque than the PS-FRPM-SPM and PS-FRPM-RPM machines, due to similar PM pole-pair number and iron piece number.

(4) The PS-FRPM-SPM and MG-SPM machines have higher average torque than the PS-FRPM-RPM and MG-RPM machines at the rated condition. However, the MG-SPM machine is easier to be saturated than the PS-FRPM-SPM machine, due to the thinner iron pieces. The PS-FRPM-RPM machine suffers from the highest torque ripple due to the unbalanced magnetic circuit and high cogging torque. The MG-RPM machine has the smallest torque ripple, resulting from the low back-EMF harmonics and also the small cogging torque.

(5) The MG-SPM and MG-RPM machines suffer from higher iron loss than the PS-FRPM-SPM and PS-FRPM-RPM machines, due to the higher electric frequency. However, the MG-SPM and MG-RPM machines have less PM eddy current loss as a result of the smaller PM bulk volumes. The PS-FRPM-SPM and MG-RPM machines have higher efficiency than the PS-FRPM-RPM and MG-SPM machines, due to the larger average torque.

(6) All the four analyzed machines have similar d- and q-axis inductances and hence the negligible reluctance torque. The PS-FRPM-SPM and PS-FRPM-RPM machines have higher power factor than the MG-SPM and MG-RPM machines, due to the less flux-leakage.

Overall, in designing a MG machine for various applications, two general design guides regarding: (a) a SPM or RPM type machine and (b) a higher or smaller gear ratio machine are given as follows, respectively.

(1) A SPM type machine is recommended to enhance the electric frequency, and hence phase back-EMF and torque.

(2) As for EVs or HEVs, a smaller gear ratio machine is preferred to reduce the flux-leakage for obtaining a higher power factor and a smaller iron loss, albeit with a slightly higher PM eddy current loss. However, if a lower cogging torque and a smaller torque ripple are desired, higher gear ratio machines are recommended for wind turbines and motion control applications.

REFERENCES

[1] Z. Q. Zhu, and D. Howe, "Electrical machines and drives for electric, hybrid and fuel cell vehicles," *Proc. IEEE*, vol. 95, no. 4, pp. 746-765, Apr. 2007.

[2] K. T. Chau, C. C. Chan, and C. H. Liu, "Overview of permanent-magnet brushless drives for electric and hybrid electric vehicles," *IEEE Trans. Ind. Electron.*, vol. 55, no. 6, pp. 2246-2257, Jun. 2008.

[3] M. Cheng, W. Hua, J. Zhang, and W. Zhao, "Overview of stator-permanent magnet brushless machines," *IEEE Trans. Ind. Electron.*, vol. 58, no. 11, pp. 5087-5101, Nov. 2011.

[4] T. M. Jahns, G. B. Kliman, Thomas W. Neumann, "Interior permanent-magnet synchronous motors for adjustable-speed drives," *IEEE Trans. Ind. Appl.*, vol. IA-22, no. 4, pp. 738-747, Jul. 1986.

[5] N. Bianchi, and S. Bolognani, "Design techniques for reducing the cogging torque in surface-mounted PM motors," *IEEE Trans. Ind. Appl.*, vol. 38, no. 5, pp. 1259-1265, Sep./Orc. 2002.

[6] A. M. El-Refaie, T. M. Jahns, and D. W. Novotny, "Analysis of surface permanent magnet machines with fractional-slot concentrated windings," *IEEE Trans. Energy Convers.*, vol. 21, no. 1, pp. 34-43, Mar. 2006.

[7] J. Cros, and P. Viarouge, "Synthesis of high performance PM motors with non-overlapping windings," *IEEE Trans. Energy Convers.*, vol. 17, no. 2, pp. 248-253, Jun. 2002.

[8] Z. Z. Wu, and Z. Q. Zhu, "Analysis of air-gap field modulation and magnetic gearing effects in switched flux permanent magnet machines," *IEEE Trans. on Magn.*, vol. 51, no. 5, pp. 1-12, May 2015, Art. ID 8105012.

[9] M. Freddy, and L. Heinz, "Parasitic effects in PM machines with concentrated windings," *IEEE Trans. Ind. Appl.*, vol. 43, no. 5, pp. 1223–1232, Sep./Oct. 2007.

[10] R. Qu, D. Li, and J. Wang, "Relationship between magnetic gears and vernier machines," in *Proc. Int. Conf. Electr. Mach. Syst.*, Beijing, China, 2011, pp. 1-6.

[11] J. Li, K. T. Chau, and W. Li, "Harmonic analysis and comparison of permanent magnet vernier and magnetic-geared machines," *IEEE Trans. Magn.*, 47, no. 10, pp. 3649-3652, Oct. 2011.

[12] S. L. Ho, S. Niu, and W. N. Fu, "Design and comparison of vernier permanent magnet machines," *IEEE Trans. Magn.*, vol. 47, no. 10, pp. 3280-3283, Oct. 2011.

[13] D. Li, R. Qu, W. Xu, J. Li, and T. A. Lipo, "Design procedure of dual-stator, spoke-array vernier permanent magnet machines," *IEEE Trans. Ind. Appl.*, vol. 51, no. 4, pp. 2972-2983, Jul.-Aug. 2015.

[14] K. Atallah, and D. Howe, "A novel high-performance magnetic gear," *IEEE Trans. Magn.*, vol. 37, no. 4, pp. 2844-2846, Jul. 2001.

[15] K. Atallah, S. D. Calverley, and D. Howe, "Design, analysis and realisation of a high-performance magnetic gear," *IEE Proc. Electric Power Appl.*, vol. 151, no. 2, pp. 135-143, Mar. 2004.

[16] P. O. Rasmussen, T. O. Andersen, F. T. Jorgensen, and O. Nielsen, "Development of a high-performance magnetic gear," *IEEE Trans. Ind. Appl.*, vol. 41, no. 3, pp. 764-770, May-Jun. 2005.

[17] L. N. Jian, and K. T. Chau, "A coaxial magnetic gear with Halbach permanent-magnet arrays," *IEEE Trans. Energy Convers.*, vol. 25, no. 2, pp. 319-328, Jun. 2010.

[18] L. Wang, J. Shen, Y. Wang, and K. Wang, "A novel magnetic-geared outer-rotor permanent-magnet brushless motor," in *Proc. of Power Electro. Mach. and Dri.*, Yoke, UK, 2008. pp. 33-36.

[19] K. Atallah, J. Rens, S. Mezani, and D. Howe, "A novel "Pseudo" direct-drive brushless permanent magnet machine," *IEEE Trans. Magn.*, vol. 44, no. 11, pp. 4349-4352, Nov. 2008.

[20] L. Li, W. N. Fu, and S. L. Ho, S. Niu, and Y. Li, "A quantitative comparison study of power-electronic-driven flux-modulated machines using magnetic field and thermal field co-simulation," *IEEE Trans. Ind. Electron.*, vol. 62, no. 10, pp. 6076-6084, Oct. 2015.

[21] K. T. Chau, D. Zhang, J. Z. Jiang, C. Liu and Y. Zhang, "Design of a magnetic-geared outer-rotor permanent-magnet brushless motor for electric vehicles," *IEEE Trans. Magn.*, vol. 43, no. 6, pp. 2504-2506, Jun. 2007.

[22] K. Atallah, J. Wang, S. D. Calverley, and S. Duggan, "Design and operation of a magnetic continuously variable transmission," *IEEE Trans. Ind. Appl.*, vol. 48, no. 4, pp. 1288-1295, Jul.-Aug. 2012.

[23] A. Penzkofer, and K. Atallah, "Analytical modeling and optimization of pseudo-direct drive permanent magnet machines for large wind turbines," *IEEE Trans. Magn.*, vol. 51, no. 12, Dec. 2015, Art. ID 8700814.

[24] L. Jian, K. T. Chau, and J. Z. Jiang, "A magnetic-geared outer-rotor permanent-magnet brushless machine for wind power generation," *IEEE Trans. Ind. Appl.*, vol. 45, no. 3, pp. 954-962, May-Jun. 2009.

[25] R. Montague, C. Bingham, and K. Atallah, "Servo control of magnetic gears," *IEEE/ASME Trans. Mech.*, vol. 17, no. 2, pp. 269-278, Apr. 2012.

[26] S. Gerber, and R. Wang, "Design and evaluation of a magnetically geared PM machine," *IEEE Trans. Magn.*, vol. 51, no. 8, Art. ID 8107010, Aug. 2015

[27] J. M. Crider, and S. D. Sudhoff, "An inner rotor flux-modulated permanent magnet synchronous machine for low-speed high-torque applications," *IEEE Trans. Energy Convers.*, vol. 30, no. 3, pp. 1247-1254, Sep. 2015.

[28] Q. Wang, and S. Niu, "A novel hybrid-excited dual-PM machine with bi-directional flux modulation," *IEEE Trans. Energy Convers.*, in press.

[29] S. Mezani, T. Hamiti, L. Belguerras, T. Lubin, M. Rashed, and C. Gerada, "Magnetically geared induction machines," *IEEE Trans. Magn.*, vol. 51, no. 11, Art. ID 8111404, Nov. 2015.

[30] Y. Liao, F. Liang, and T. A. Lipo, "A novel permanent-magnet motor with doubly-salient structure," *IEEE Trans. Ind. Appl.*, vol. 31, pp. 1069-1078, Sep./Oct. 1995.

[31] M. Cheng, K. T. Chau, and C. C. Chan, "Static characteristics of a new doubly salient permanent magnet motor," *IEEE Trans. Energy Convers.*, vol. 16, no. 1, pp. 20-25, Mar. 2001.

[32] E. Hoang, A. H. Ben Ahmed, and J. Lucidarme, "Switching flux permanent magnet polyphased synchronous machines," in *Proc. Eur. Power Electron. Conf.*, Trondheim, Norway, 1997, vol. 3, pp. 903-908.

[33] Z. Q. Zhu, Y. Pang, D. Howe, S. Iwasaki, R. Deodhar, and A. Pride, "Analysis of electromagnetic performance of switched flux switching permanent magnet machines by non-linear adaptive lumped parameter magnetic circuit model," *IEEE Trans. Magn.*, vol. 41, no. 11, pp. 4277-4287, Nov. 2005.

[34] W. Hua, M. Cheng, Z. Q. Zhu, and D. Howe, "Analysis and optimization of back EMF waveform of a flux-switching permanent magnet motor," *IEEE Trans. Energy Convers.*, vol. 23, no. 3, pp. 727-733, Sep. 2008.

[35] W. Zhao, M. Cheng, W. Hua, H. Jia, and R. Cao, "Back-EMF harmonic analysis and fault-tolerant control of flux-switching permanent-magnet machine with redundancy," *IEEE Trans. Ind. Electron.*, vol. 58, no. 5, pp. 1926-1935, May 2011.

[36] R. Cao, C. Mi, and M. Cheng, "Quantitative comparison of flux-switching permanent-magnet motors with interior permanent magnet motor for EV, HEV and PHEV applications," *IEEE Trans. Magn.*, vol. 48, no. 8, pp. 2374-2384, Aug. 2012.

[37] G. Zhang, W. Hua, M. Cheng, B. Zhang, and X. Guo, "Coupled magnetic-thermal fields analysis of water cooling flux-switching permanent magnet motors by an axially segmented model," *IEEE Trans. Magn.*, in press.

[38] C. Yu, and S. Niu, "Development of a magnetless flux switching machine for rooftop wind power generation," *IEEE Trans. Energy Convers.*, vol. 30, no. 4, pp. 1703-1711, Dec. 2015.

[39] D. Li, R. Qu, J. Li, W. Xu, and L. Wu, "Synthesis of flux switching permanent magnet machines," *IEEE Trans. Energy Convers.*, vol. 31, no. 1, pp. 106-117, Mar. 2016.

[40] C. X. Wang, I. Boldea, and S. A. Nasar, "Characterization of three phase flux reversal machine as an automotive generator," *IEEE Trans. Energy Convers.*, vol. 16, no. 1, pp. 74-80, Mar. 2001.

[41] D. S. More, and B. G. Fernandes, "Analysis of flux-reversal machine based on fictitious electrical gear," *IEEE Trans. Energy Convers.*, vol. 25, no. 4, pp. 940-947, Dec. 2010.

[42] C. H. T. Lee, K. T. Chau, and C. Liu, "Design and analysis of a cost-effective magnetless multiphase flux-reversal DC-field machine for wind power generation," *IEEE Trans. Energy Convers.*, vol. 30, no. 4, pp. 1565-1573, Dec. 2015.

[43] Z. Q. Zhu, Z. Z. Wu, D. J. Evans, and W. Q. Chu, "Novel electrical machine having separate PM excitation stator," *IEEE Trans. Magn.*, vol. 51, no. 4, Art. ID 8104109, Apr. 2015.

[44] S. J. Arand, and M. Ardebili, "Multi-objective design and prototyping of a low cogging torque axial-flux PM generator with segmented stator for small-scale direct-drive wind turbines," *IET Elec. Power Appl.*, vol. 10, no. 9, pp. 889-899, Nov. 2016.

[45] T. M. Jahns, and W. L. Soong, "Pulsating torque minimization techniques for permanent magnet AC motor drives - a review," *IEEE Trans. Ind. Electron.*, vol. 43, no. 2, pp. 321-330, Apr. 1996.

[46] Z. Q. Zhu, "A simple method for measuring cogging torque in permanent magnet machines," in *Rec. of IEEE-PES Gener. Meeting*, Calgary, Canada, Jul. 2009, pp. 1-4.

[47] X. Liu, and Z. Q. Zhu, "Electromagnetic performance of novel variable flux reluctance machines with DC-field coil in stator," *IEEE Trans. Magn.*, vol. 49, no. 6, pp. 3020-3028, Jun. 2013.

[48] S. Wiesember, A. Proca, and A. Keyhani, "Estimation of permanent magnet motor parameters," in *Rec. of IEEE-IAS Annu. Meeting*, New Orleans, US, 1997, vol. 1, pp. 29-34.
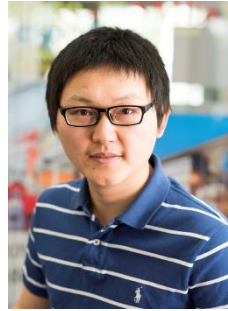
Zhongze Wu was born in Yancheng, China, in 1988. He received the B.Eng. and M.Sc. degrees in electrical engineering from the Chien-Shiung Wu College and the School of Electrical Engineering, Southeast University, Nanjing, China, in 2010 and 2013, respectively, and the Ph.D. degree in electrical and electronic engineering from The University of Sheffield, Sheffield, U.K., in 2017.

Since 2017, he has been with Warwick Manufacturing Group (WMG), The University of Warwick, where he is currently a research fellow. His major research interests include the analysis, design and manufacturing of synchronous machines and magnetic gear for electrical vehicle and wind power generation applications.

Dr. Wu served as secretary at IEEE Sheffield University Student Branch Joint IAS/PELS Chapter from August 2016.

Z. Q. Zhu (M'90–SM'00–F'09) received the B.Eng. and M.Sc. degrees in electrical and electronic engineering from Zhejiang University, Hangzhou, China, in 1982 and 1984, respectively, and the Ph.D. degree in electrical and electronic engineering from The University of Sheffield, Sheffield, U.K., in 1991.

Since 1988, he has been with The University of Sheffield, where he is currently a Professor with the Department of Electronic and Electrical Engineering and the Head of the Electrical Machines and Drives Research Group. He is a Fellow of the Royal Society of Engineering. His current major research interests include the design and control of permanent-magnet brushless machines and drives for applications ranging from automotive to renewable energy.
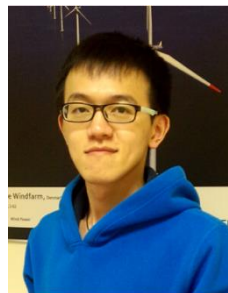
Hanlin Zhan (S'16) received the B.Eng. and the M.Sc. degrees in Electrical Engineering from Harbin Institute of Technology, Harbin, China, in 2012 and 2014, respectively. He is currently working toward Ph.D. degree with the Department of Electronics and Electrical Engineering, the University of Sheffield, Sheffield, U.K.

His current research interests include permanent magnet synchronous motor drives and parameter identification.